Article

DNA Capture by Nanopore Sensors under Flow

Ali Najafi Sohi, Eric Beamish, Vincent Tabard-Cossa, and Michel Godin

Anal. Chem., **Just Accepted Manuscript** • DOI: 10.1021/acs.analchem.9b05778 • Publication Date (Web): 15 May 2020

DNA Capture by Nanopore Sensors under Flow

Ali Najafi Sohi,[†] *Eric Beamish,*[†] *Vincent Tabard-Cossa,*[†] *and Michel Godin*[†,‡,§,]*

[†]Department of Physics, [‡]Department of Mechanical Engineering, and [§]Ottawa-Carleton Institute for Biomedical Engineering, University of Ottawa, Ottawa, Ontario K1N 6N5, Canada

KEYWORDS: nanopore, microfluidics, capture rate, translocation, capture volume

Corresponding Author

*E-mail: michel.godin@uottawa.ca.

ABSTRACT. Integrating nanopore sensors within microfluidic architectures is key to providing advanced sample processing capabilities upstream of the biosensor. When confined in a microchannel, the nanopore capture and translocation characteristics are altered when subjected to cross-flow, affecting sensor performance. Here, we study the capture rate and translocation of 1–5 kbp double-stranded DNA molecules through solid-state nanopores in the presence of tangential fluid flow over the nanopore aperture. Experiments reveal a trend of increased capture rate with cross-flow, reaching a 5-fold enhancement (dependent on DNA length) at moderate flow rates, before decreasing at higher flow rates. By modeling DNA dynamics in microchannels under the combined effect of laminar flow, Brownian motion and electrophoretic drift, it is shown that the

observed trend is the result of two competing mechanisms: enhanced DNA transport by convection and reduction in the nanopore's capture volume with increased flow velocity. Moreover, it is shown that the viscous drag force exerted by flow on a translocating DNA can be exploited to tune the kinetics of DNA translocation.

1. INTRODUCTION.

Solid-state nanopores, realized as nanometer-scale holes in thin membranes, have attracted significant interest as single molecule sensors for probing DNA, proteins and biomolecular interactions [1,2]. As biomolecules, such as DNA, typically carry electrical charge in solution, the application of an electric field across the membrane captures and electrophoretically forces the molecule to translocate through the nanopore. During this molecular translocation, the steric displacement of ions results in a measurable transient shift in the ionic current passing through the nanopore. The amplitude and duration of this current shift reveal information about the biomolecule's conformation and size, and its interaction with the nanopore [3,4].

Recently, the application of the controlled breakdown (CBD) method for *in situ* fabrication of nanopores in aqueous environment [5–7] has facilitated the integration of solid-state nanopores within microfluidic networks [8,9]. Such integration offers the potential for bridging the advantages of both platforms, including reduced sample consumption [10], increased analysis speed [11], higher throughput via multiplexing [8], enhanced transport of target molecules by convection to overcome the limitations of diffusion [12–15], and sensing with single molecule sensitivity [1]. Despite numerous efforts to build and operate such integrated systems, a comprehensive understanding of nanopore capture and passage characteristics in the presence of

a tangential fluid flow over the nanopore aperture (cross-flow) is lacking. Here, we construct an integrated nanopore-microfluidic device to investigate the effects of cross-flow on nanopores by exploring how the two main performance metrics of nanopores, capture rate (J) and translocation time of DNA (τ), vary with cross-flow. To substantiate our experimental findings, we develop an analytical model to investigate the intricate interplay of convection, diffusion and electrophoretic drift near the nanopore. We use this model to investigate the effective capture volume of a nanopore in the presence of cross-flow and to explain the experimentally observed flow-dependent capture rate of nanopores. Furthermore, we model the translocation kinetics of DNA subjected to a lateral hydrodynamic drag force exerted by the cross-flow. We use this model to elucidate the underlying physics of flow-dependent DNA translocation time.

2. RESULTS AND DISCUSSION.

2.1 Integrated Nanopore-Microfluidic Device.

The integrated nanopore-microfluidic device designed and fabricated to investigate the effect of cross-flow on nanopore sensing characteristics is depicted in Figure 1 (see also Figure S1). The device includes a silicon (Si) chip that supports a silicon nitride (SiN) membrane at its center. The Si chip is interfaced with two microfluidic channels realised in polydimethylsiloxane (PDMS) using soft lithography techniques. Once the microfluidic networks are filled with solutions, the SiN membrane forms a nonconductive barrier separating the two microchannels. In Figure 1a, the top microchannel ("top side") has cross sectional dimensions of width × height = 100×70 μm^2 and carries a flow adjacent to the membrane. The underside of the membrane ("bottom side", Figure 1 and S1) is centered in the etch cavity of the Si chip, which meets a

lower microchannel (not depicted in Figure 1 but visible in Figure S2) that does not include cross-flow in our experiments. Holes punched in the PDMS provide fluidic and electrical access to the microchannels, Figure 1a. More information on the design and fabrication of the device could be found in the Experimental Section as well as in Note 1, Supporting Information.

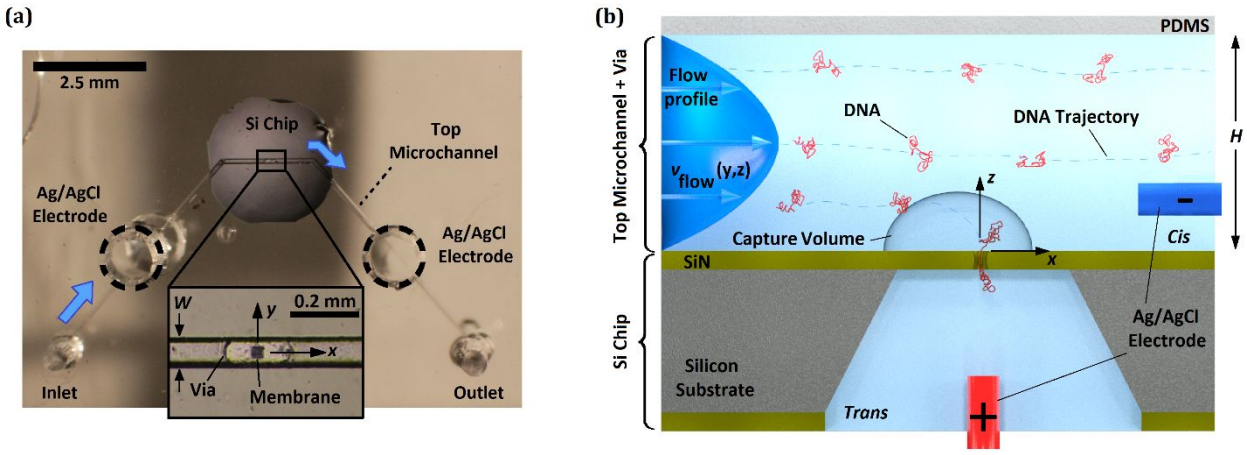

Figure 1. (a) Top view of the integrated nanopore-microfluidic device showing the Si chip, SiN membrane, top microchannel, and punched holes for inlet/outlet to microchannel (0.75 mm in diameter) and electrodes (1.25 mm in diameter); inset shows the top via assembled around the SiN membrane. (b) Depiction of the experimental case where DNA molecules flow through the top microchannel, and the cross-flow enhances molecular transport into capture volume around the nanopore. The asymmetrical shape of the capture volume (not to scale), stretched in the upstream direction, is a result of flow in the microchannel. Outside the capture volume, the combination of flow velocity (directional) and diffusion (random direction) determines the trajectory of DNA molecules (dashed lines). Once DNA enters the capture volume, the electrophoretic force dominates over flow and diffusion, and results in DNA capture by the nanopore.

For *in situ* fabrication of nanopores, we followed CBD protocols which involve imposing high electric fields until a nanopore is created [5,7,8]. The experimental setup and nanopore

fabrication protocols are described in more detail in the Experimental Section and in Note 2 and 3, Supporting Information.

DNA samples were prepared by mixing 1, 2, or 5 kbp double-stranded DNA (dsDNA) molecules in 3.6 M LiCl, pH 10, to a final DNA concentration of $c = 1.9 - 10$ nM (Note 4, Supporting Information). The DNA sample was sent through the corresponding microchannel by inducing a pressure-driven Poiseuille flow (Note 5, Supporting Information).

To provide a thorough understanding of the effect of cross-flow on nanopores, two (complementary) sets of experiments were performed. In the first set, DNA was introduced in the microchannel on the top side of the nanopore, where cross-flow was present, Figure 1b. In the second set, DNA was introduced within the microchannel on the bottom side of the membrane, *i.e.* through the etch cavity in the Si chip, where the cross-flow velocity is zero. DNA capture and translocation through the nanopore was initiated by applying a transmembrane potential ΔV of 200 mV (1 kbp) or 400 mV (2 and 5 kbp). Transient current blockages upon DNA translocation were measured using a low-noise current amplifier (see Experimental Section and Note 2, Supporting Information).

2.2 Molecular Capture under Cross-Flow

A baseline molecular capture rate, J_0, and a mean translocation time, τ_0, measured with no cross-flow were subsequently used to normalize the corresponding results from the experiments carried out in the presence of increasing cross-flow. As results were repeated using multiple nanopores to test consistency, this normalization facilitated the comparison of results acquired using different nanopores by mitigating potential inter-nanopore variability, which has been shown to exist even when nanopore dimensions (diameter and membrane thickness) and sensing

conditions (sensing voltage, salt concentrations, etc.) are kept consistent between experiments [16]. The cross-flow above the nanopore was induced by sustaining a pressure-driven Poiseuille flow in the top microchannel with volumetric flow rate Q up to 38 μL min $^{-1}$, corresponding to a Reynolds number of up to 10 [17,18]. Assuming the no-slip boundary condition, the fluid velocity profile in the top microchannel is given by [19]

$$\vec{v}_{flow}(y,z) = \frac{48Q}{WH\pi^3}\left\{1 - \sum_{n=1,3,5}^{\infty}\left[\frac{192H}{n^5\pi^5 W}\tanh\left(\frac{n\pi W}{2H}\right)\right]\right\}^{-1} \times \sum_{n=1,3,5}^{\infty}\left\{\frac{\sin\left(\frac{n\pi z}{H}\right)}{n^3}\left[1 - \frac{\cosh\left(\frac{n\pi y}{H}\right)}{\cosh\left(\frac{n\pi W}{2H}\right)}\right]\right\}\hat{x} \quad (1)$$

where $H = 70$ μm is the total microchannel height above the nanopore and $W = 100$ μm is the total microchannel width above the pore, Figure 1. In our analytical model, the origin of the coordinate system is at the center of the SiN membrane's top side, so that $-0.5W \leq y \leq 0.5W$ and $0 \leq z \leq H$. For simplicity, we assume that the nanopore is at the center of the SiN membrane and the origin of the coordinate system is at the center of its mouth, Figure 1b. In the absence of cross-flow, the capture radius of the nanopore, r^*, is defined as the maximum distance from the nanopore where the electrophoretic force generated by the trans-membrane potential overcomes the Brownian motion of DNA [16,20–22]. In high molarity LiCl, for the range of pore sizes and applied voltages used here, it is of the same order of magnitude as the radius of gyration of the DNA studied [21,23]. However, when there is cross-flow, the pore electrophoretic capture force has to prevail not only over the Brownian motion of DNA but also over the convective flow, which tends to sweep DNA away from the sensing site [14]. As such, we use the (dimensionless) Peclet number of the microchannel, defined as $\mathrm{Pe} = Q/DW$ where D is the diffusion coefficient

of DNA, to represent the interplay between convection and diffusion in the vicinity of the nanopore. Using the Peclet number enables us to generalize our findings to other DNA molecules (different diffusion behavior) and/or microchannel geometries. The relatively small capture range of the nanopore (in comparison to the characteristic dimensions of the microchannel next to it) suggests that the effect of cross-flow on nanopore performance is limited to a thin layer adjacent to the nanopore (with Equation 1 describing the velocity profile), rather than the entire cross-section of the microchannel. However, for simplicity and without loss of generality, we present our findings, and draw conclusions, by using Peclet number and volumetric flow rate to represent the cross-flow. Of course, considering the stochastic nature of nanopore creation by the CBD method [5,24], and the 50×50 μm size of the SiN membrane interfaced with 100 μm wide microchannel, an uncertainty of up to 15% in the determination of flow velocity adjacent to the nanopore's aperture is expected (Note 6, Supporting Information).

2.3 Capture Rate Enhancement

The nanopore's capture rate depends on cross-flow through the microchannel. Figure 2 shows representative examples where 5 kbp dsDNA ($c = 2.4$ nM) was sensed by nanopores ($\Delta V = -400$ mV) in three different devices. In one set of results obtained on a single device, ten experiments were carried out with $0 \leq Q \leq 23$ μL min^{-1}. Figure 2a shows representative 30-second baseline recordings for the experiments with $Q = 0$ (no cross-flow), $Q = 10$ μL min^{-1} and $Q = 23$ μL min^{-1}. The ionic current spikes in Figure 2a correspond to individual DNA translocation events. Data was acquired for 10-20 minutes under each flow condition.

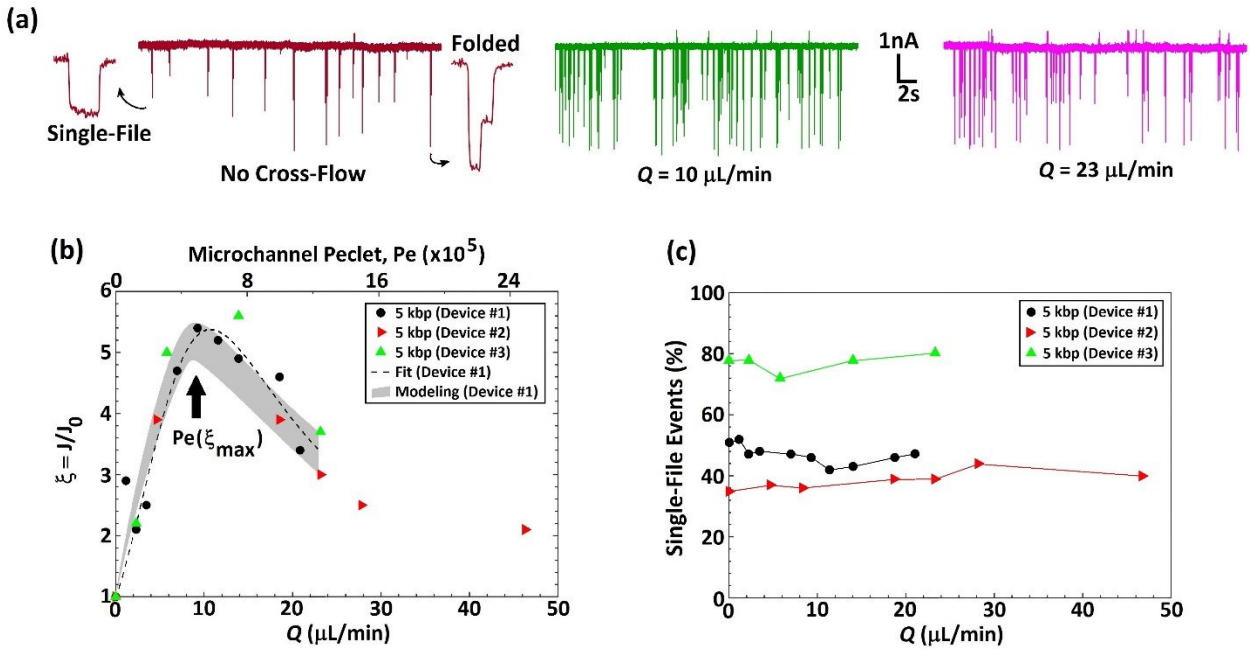

Figure 2. Effect of cross-flow on 5 kbp ds-DNA sensing. (a) Representative 30-second baseline recordings under different volumetric flow rates: (left) $Q = 0$, (middle) $Q = 10\ \mu\text{L min}^{-1}$ $(\text{Pe} = 4 \times 10^5)$, (right) $Q = 23\ \mu\text{L min}^{-1}$ $(\text{Pe} = 9 \times 10^5)$. Insets in the left panel represent single-file and folded translocation events. (b) Variation of normalized capture rate, $\xi = \text{J}/\text{J}_0$, with volumetric flow rate (Q) and Peclet number of the top microchannel (Pe). Three independent experiments performed on different devices (nanopore diameters $d_1 = 9\ nm$, $d_2 = 6\ nm$ and $d_3 = 8\ nm$; $\Delta\text{V} = -400$ mV.) are shown. The dashed line is a rational function fit to experimental data. The grey band is the prediction by numerical simulation with the consideration of the uncertainties associated with the diffusion coefficient and electrophoretic mobility of 5 kbp dsDNA. (c) The ratio of single-file translocation events to the total number of translocation events is used as an indicator of DNA conformation upon arrival at the nanopore. The relative constancy of this ratio as a function of cross-flow, suggests that the molecular configuration of DNA does not change significantly with flow. The lines linking data points are to guide the eye.

For each flow rate, the frequency of capture was extracted from exponential fits to the normalized distributions of the elapsed time between successive translocation events (see Note 7,

Supporting Information) [16,25]. The variation in capture rate with flow velocity in the top microchannel is summarized in Figure 2b where the normalized capture rate $\xi = J/J_0$ is shown as a function of volumetric flow rate and the Peclet number. The sets of experiments were repeated on three different devices under similar conditions. The capture rate followed an initial increase with flow velocity, reaching a maximum value of ξ_{max}~5.3 at $Q \approx 10$ μL min^{-1} $(\mathrm{Pe} = 4 \times 10^5)$, and then dropped upon further increasing the flow rate. The dashed line in Figure 2b is a rational function fit to the experimental data. The grey band in Figure 2b shows the trend in capture rate variation with flow rate as predicted by numerical simulations with the consideration of the uncertainties associated with diffusion coefficient and electrophoretic mobility of 5 kbp dsDNA (Note 8, Supporting Information). Figure 3 reveals a similar trend in the capture rate, for two different DNA lengths, with ξ_{max}~2.7 $(Q \approx 23.5$ μL min^{-1}, $\mathrm{Pe} = 4.1 \times 10^5)$ for 1 kbp and ξ_{max} ~3.9 $(Q \approx 16.3$ μL min^{-1}, $\mathrm{Pe} = 4.05 \times 10^5)$ for 2 kbp dsDNA.

The observed enhancement in capture rate due to improved DNA transport, i.e. synergy between diffusion and convection, may also have a contribution from the flow-induced variation in molecular configuration of DNA. To gauge the relative importance of this effect, we argue that one would also expect to observe variations in the folded fraction of events (i.e. the ratio of single-file translocation events to the total number of translocations) as an indicator of DNA conformation prior to capture [26]. Figure 2c shows that while this ratio was different for experiments conducted on different devices, it did not change throughout a given experiment despite varying flow rates. This suggest that, within the range of flow velocity and DNA lengths used in this work, no noticeable change in DNA configuration, e.g. pre-stretching due to shear flow, has occurred [27].

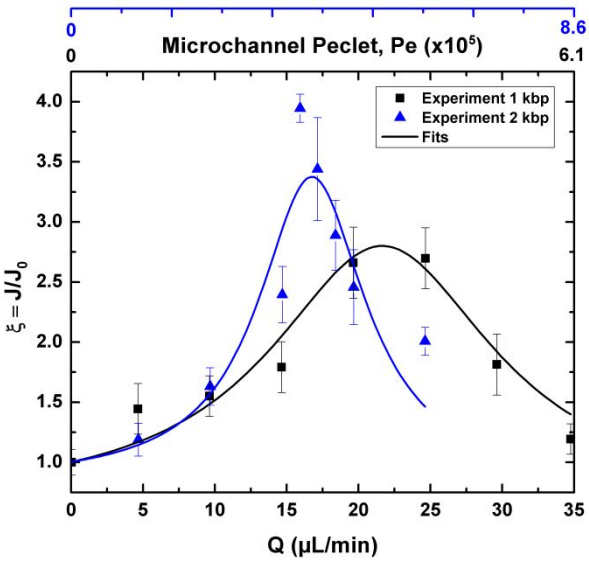

Figure 3. Variation of normalized capture rate, $\xi = J/J_0$, with volumetric flow rate (Q) and Peclet number of the top microchannel (Pe) for (■) 1 kbp ($d = 8$ nm, $\Delta V = -200$ mV) and (▲) 2 kbp dsDNA ($d = 6$ nm, $\Delta V = -400$ mV). Lines are rational function fits to experimental data, as guides to the eye. The Peclet numbers corresponding to the maximum of ξ (similar for both experiments) can also be inferred using the top axis. Capture rates were evaluated by measuring a minimum of 200 molecular translocation events at each flow rate, while errors bars represent standard errors.

Many nanopore-based bioassays rely on counting individual molecules for detection and quantification of biomarkers [16,28]. When counting a fixed number of single molecules, increasing the capture rate translates to a decrease in measurement time, which is particularly important in the rapid concentration quantification of low abundance samples. Nanopore capture rate enhancements have been reported before using a variety of approaches, including modification of solution temperature (ξ_{max}~2.9 through heating the nanopore flow cell

uniformly by $\Delta T = 40$ ℃) [29] and maintaining a salt concentration gradient across the nanopore (ξ_{max}~40 using a 32-fold salt gradient) [20]. The DNA-size dependent enhancement in capture rate of 3 to 5-fold reported in this work introduces a new means to improve the measurement throughput of nanopore sensors that can be combined with other approaches to achieve 10 to 100-fold capture rate enhancement.

The experimental results presented in Figures 2b and 3 reveal several interesting trends. First, there is a limit on how much the capture rate of a nanopore could be enhanced by convection. We hypothesize that this is due to two competing mechanisms: enhanced DNA transport by convection and reduction in nanopore's capture volume with increased cross-flow (more on this below). Secondly, the maximum enhancement in capture rate increases with the size of DNA, which could be due to the fact that larger DNA molecules have a lower diffusion constant; thus, convection could play a bigger role in effectively transporting such molecules into the sensing region around the nanopore. Thirdly, the volumetric flow rate associated with the maximum capture rate decreases with the size of DNA. Interestingly, when Peclet number is used to represent the flow rate in microchannel (Figure 3), all the capture rate maxima appear at $\mathrm{Pe} = (4.05 \pm 0.05) \times 10^5$, suggesting that a balance between diffusion and convection is likely the reason behind this trend.

2.4 Analytical Model

In supporting these observations, complementary numerical simulations we carried out to unravel the collective dynamics of DNA in these integrated nanopore-microfluidic systems under the combined effect of Brownian motion, pressure-driven laminar flow and electrophoretic drive.

The application of the DC sensing voltage ΔV across the SiN membrane can be modeled by an electric field that extends radially from the nanopore mouth into the microchannel [30]. Consider a negatively charged DNA molecule momentarily located at $\vec{s} = (x\hat{x}, y\hat{y}, z\hat{z})$ in the top microchannel, where $\hat{x}$, $\hat{y}$ and $\hat{z}$ are the unit vectors of the coordinate system. As a result of the electric field, over a sufficiently small time step Δt, the DNA will electrophoretically drift toward the nanopore by

$$\overrightarrow{\Delta s_{ep}} = \frac{-\mu_e \Delta V \Delta t \, d^2}{8lr^3}\vec{s} \quad (2)$$

where μ_e, $r = |\vec{s}|$, d and l represent the electrophoretic mobility of DNA, momentary distance of DNA from nanopore, nanopore diameter and membrane thickness, respectively. Neglecting inertial effects, the diffusive motion of DNA during the time step Δt is modeled as [31]

$$\overrightarrow{\Delta s_{diff}} = \sqrt{2D\Delta t}(w_x\hat{x} + w_y\hat{y} + w_z\hat{z}) \quad (3)$$

where w_x, w_y and w_z are random numbers selected from a Gaussian distribution with zero mean ($\mu = 0$) and a standard deviation of 1 ($\sigma = 1$). To model the hydrodynamic effects of laminar flow on DNA, we assumed that DNA travels in the direction of flow at the same speed as its surrounding fluid, i.e. no relative slippage between DNA and adjacent streamlines [32]. Using the velocity profile of pressure-driven Poiseuille flow given in Equation 1, the corresponding convective displacement of the DNA molecule can be calculated by

$$\overrightarrow{\Delta s_{flow}} = \vec{v}_{flow}\Delta t \quad (4)$$

The electrophoretic, diffusive and convective displacement fields act upon DNA concurrently and in a coupled manner. To get an approximate yet sensible picture of DNA dynamics in the microchannel, the governing equations were solved incrementally and the results were summed

to determine DNA position after each time step. The DNA concentrations in the range of 1.9-10 nM used in our experiments were low enough to preclude the possibility of entangled DNA molecules which would result in restricted self-diffusion [33], yet were high enough to avoid sample depletion near the nanopore upon translocation. The latter was evidenced by the stable capture rates recorded under different flow conditions, irrespective of the duration of experiment. Given the results in Figure 2c, DNA molecules were assumed to have constant hydrodynamic properties, namely D and μ_e, at the flow rates used in this study. We first look into how capture volume changes with flow velocity in the microchannel. In the absence of flow, the capture volume takes the expected shape of a hemisphere with radius r^*, as schematically illustrated in Figure 4a. Throughout our simulations, the capture volume is defined as the region around the nanopore where the probability of DNA capture, ε_{cap}, is more than 50%.

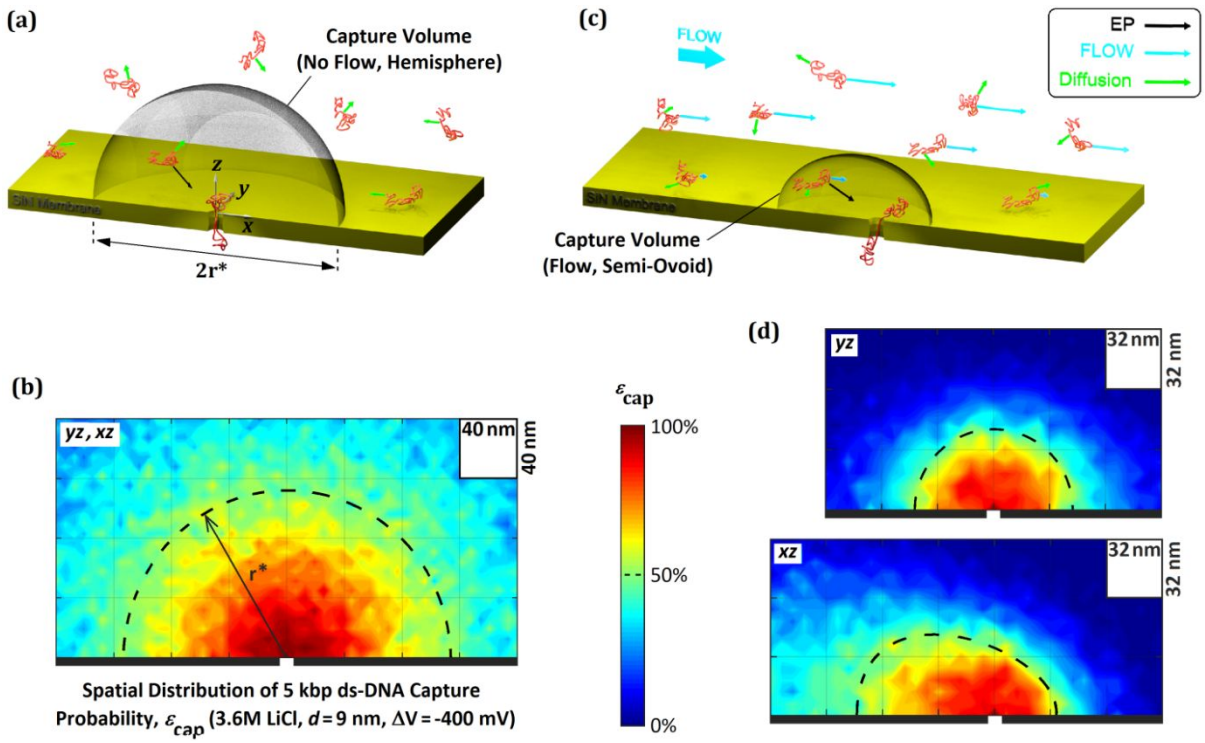

Figure 4. (a) In the absence of flow, DNA molecules diffuse into the hemispherical capture volume, with capture range r^* around the nanopore, where they are electrophoretically captured by the nanopore. (b) Spatial distribution of DNA capture probability, ε_{cap}, in the *yz* plane predicted by simulations for the representative case of 5 kbp dsDNA sensed by a 9 nm nanopore using a sensing voltage of $\Delta V = -400$ mV. (c) In the presence of cross-flow, the size of the capture volume is reduced and its shape changes from symmetric hemispheric, as in (a), to asymmetric semi-ovoid skewed in the upstream direction. (d) Spatial probability of DNA capture along the *yz* and *xz* planes in the presence of a volumetric flow rate $Q \approx 21\ \mu L\ min^{-1}$. Other simulation parameters are the same as in (b). Dashed lines in (b) and (d) mark the approximate boundary of the capture volume where ε_{cap}~50%.

Figure 4b shows the spatial distribution of ε_{cap} in a representative case where 5 kbp dsDNA in 3.6 M LiCl buffer is sensed by a 9 nm nanopore subjected to trans-membrane potential voltage $\Delta V = -400$ mV. The simulation proposed a nearly hemispherical capture volume (marked with

thick dashed line) with $r^* \sim 113$ nm, which is in very good agreement with $r^* \sim 96$ nm predicted theoretically by [20]

$$r^* = \mu_e \Delta V \, d^2/8lD \quad (5)$$

Numerical simulations suggest that in the presence of cross-flow, the capture volume shrinks in size and its shape changes from a hemisphere to a semi-ovoid that is asymmetrically skewed in the upstream direction, as depicted in Figure 4c. As an example, Figure 4d shows the spatial distribution of DNA capture probability in the *yz* and *xz* planes for the same representative case analyzed in Figure 4b with the addition of volumetric flow rate of $Q \approx 21$ μL $\min^{-1}$ (see Note 8, Supporting Information). Compared with the results presented in Figure 4b, a 61% reduction in height (*z*-direction: from 113 to 44 nm), a 61% reduction in width (*y*-direction: from 226 to 89 nm), and a 51% reduction in length of the capture volume (*x*-direction: from 226 to 114 nm) is predicted. Such drastic changes in the size and shape of the nanopore's capture volume should be taken into account in integrated nanopore-microfluidic devices in which DNA concentration techniques like dielectrophoretic (DEP) are used to focus the DNA flow around the nanopore mouth [34].

In the presence of flow in microchannels, diffusion and convection both contribute to DNA transport into the capture volume. According to Sheehan and Whitman, the diffusive reaction rate on a 3D sensing region is proportional to its surface area [13]. Drawing analogy with a nanopore, the diffusive capture rate of the nanopore is thus expected to monotonically decrease with the increase of flow rate as the surface area of the capture volume decrease with increasing flow rate. Variation in the capture rate due to convection under increasing flow rate, on the other hand, is the result of some competing mechanisms. By increasing the flow rate, the flux of DNA

molecules actively transported into the capture volume increases. At the same time, the increase in flow rate makes the capture volume smaller, thus reducing the convective capture rate. Moreover, with a smaller capture volume, the average velocity of DNA molecules entering the capture volume decreases because of the parabolic velocity profile in microchannel and the resulting sharp velocity gradient adjacent to the nanopore. We hypothesize that the combination of these mechanisms is responsible for the trends in capture rate variation with flow rate presented in Figure 2b and 3. In a broader perspective, the physics underlying the flow-induced change in capture volume, as depicted in Figure 4, could be understood by considering the cooperative and competitive interplay between electrophoretic and hydrodynamic displacement fields near the nanopore. Given that $\Delta s_{ep} \propto r^{-2}$, the electrophoretic pull on DNA quickly diminishes away from the nanopore. In the presence of cross-flow, there is not enough time for the electrophoretic force to attract DNA molecules which are far from the nanopore before they are swept away by the flow. This results in the reduction of capture volume in comparison to the case where there is no cross-flow. Considering the direction of flow in Figure 4c, at $x < 0$, i.e. upstream of the nanopore, the electrophoretic and hydrodynamic fields both push the DNA molecule forward whereas at $x > 0$, the two force fields compete against each other. This cooperative (competitive) interaction between electrophoretic and hydrodynamic fields at $x < 0$ ($x > 0$) explains the asymmetric shape of the capture volume which stretches in the upstream direction, as exemplified in Figure 4d.

2.5 Viscous Drag

Our analysis so far has focused on DNA capture rate and its variation with cross-flow. Once captured and during translocation, a DNA molecule experiences a lateral viscous drag generated by the cross-flow on the portion of DNA in the top microchannel. If the direction of translocation

is from top to bottom, the drag force acts upon the portion of DNA (blob) remaining in the cis channel, as depicted in Figure 1b, opposing the electrophoretic threading of DNA through the nanopore. Alternatively, when DNA is loaded from the bottom side of the SiN membrane and its translocation direction is from bottom to top, the drag force will pull on the translocated part of the DNA, assisting the electrophoretic threading of DNA through the nanopore. The introduction of flow-induced drag will change the force balance on DNA. Intuitively, we expect that the new force balance on DNA affects the kinetics of translocation, specifically the translocation time of DNA through the nanopore. This is examined and validated in Figure 5 where the experimentally measured mean translocation time of single-file translocation events for 5 kbp, translocating from the top to bottom, and 2 kbp ds-DNA, translocating from bottom to top, are shown as a function of flow rate in the top microchannel.

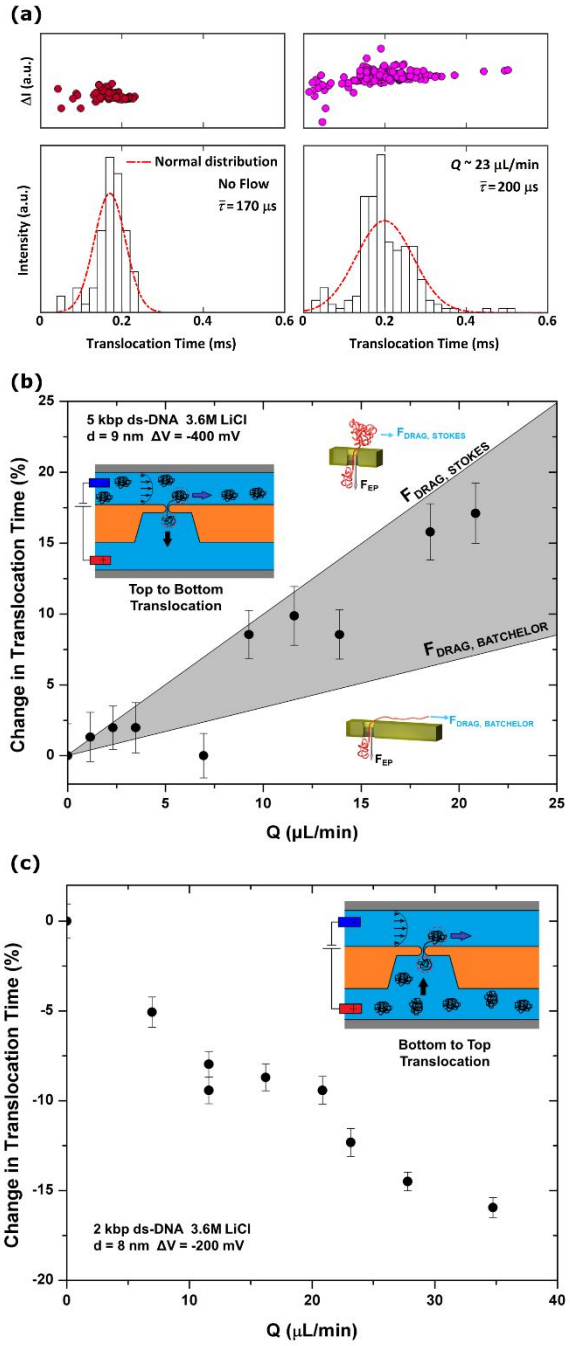

Figure 5. (a) Translocation time histograms of single-file translocation events of 5 kbp dsDNA (3.6M LiCl, $d = 9$ nm, $\Delta V = -400$ mV) in the absence of flow (left panel) and under $Q \sim 23$ μL min^{-1} (right panel). The dashed lines correspond to normal distribution fit to experimental data. As the volumetric flow rate increases, the distribution skews toward longer translocation times. (b) Relative increase in the mean translocation time, $\bar{\tau}$, of 5 kbp ds-DNA translocating from top to bottom, as a function of volumetric flow rate in the top microchannel. The grey area highlights the

theoretically predicted results for a range of DNA configurational changes, from coiled (Stokes model) to fully stretched (Batchelor model). (c) Relative decrease in average translocation time of 2 kbp dsDNA (3.6M LiCl, $d = 8$ nm, $\Delta V = -200$ mV), translocating from bottom to top, as a function of flow velocity in the top microchannel. In all cases, mean translocation times are calculated from measurements of 300-500 molecular translocation events and error bars represent standard errors.

In Figure 5a, the histograms of DNA translocation time pertaining to two experimental cases (one without flow, the other one with maximum flow rate used in the experiment) are shown along with normal distribution fits to experimental data. In the absence of cross-flow, the mean translocation time is $\bar{\tau} = 170$ μs. With the introduction of flow in the top microchannel; however, a modest stretch toward longer translocation times is observed. For the maximum volumetric flow rate of $Q \sim 23$ μL min $^{-1}$ reported in Figure 5, the mean translocation time extracted from normal distribution fit demonstrates a ~17% increase from ~ 170 μs to ~ 200 μs, although some individual events exhibited up to 100% increase in translocation time. Based on the molecular configuration of the portion of DNA (blob) remaining in the cis channel, the flow-induced drag force could be approximately modeled by the Stokes drag model for coiled DNA configuration [35], or by Batchelor drag model for fully stretched DNA configuration [36]. These models represent two extreme configurational cases, as portrayed in the insets of Figure 5b (see Note 9, Supporting Information, for more information). In reality, the blob of DNA could be partially stretched, i.e. somewhere in-between coiled and fully stretched configurations. Hence, the Stokes and the Batchelor drag forces could be looked at as the upper and lower bounds to the drag force the DNA experiences based on its molecular configuration and the flow

regime in the microchannel. Figure 5b compares the experimentally measured and these theoretically predicted relative changes in the mean translocation time of 5 kbp dsDNA (same experimental conditions as in Figure 2). The partial-stretching of tethered DNA molecules under shear flow has been previously observed in microchannels with flow velocities comparable to those used in our experiments [37,38]. Analogously, in our experiments with high flow velocities, we hypothesize that the portion of a translocating DNA molecule that remains in the microchannel experiences partial stretch because of cross-flow. Figure 5c shows the results for 2 kbp DNA translocating from the bottom side of the nanopore toward the top microchannel (experimental conditions: 3.6M LiCl, $d = 8$ nm, $\Delta V = -200$ mV). Interestingly, a reduction of ~15% in mean translocation time was observed at a maximum flow rate of $Q \sim 38$ μL min $^{-1}$. As argued before and contrary to the trend observed in Figure 5b, here, the flow-induced drag cooperates with electrophoretic force to facilitate DNA translocation through the nanopore. These findings suggest that cross-flow could be used to selectively tune (speed up or slow down) the kinetic of DNA translocation through nanopores.

3. CONCLUSION

We investigated the effect of flow, ubiquitous in microfluidic networks, on DNA capture and translocation through nanopore sensors to achieve two goals: first, to provide a comprehensive understanding of nanopore operation in the presence of tangential fluid flow (cross-flow) over the nanopore aperture, and second, to unlock the potential of fluid flow to enhance nanopore sensing performance. To those ends, we experimentally characterized the capture rates of 1–5 kbp dsDNA molecules in the presence of pressure-driven Poiseuille flow, with volumetric flow

rates up to ~38 μL min^{-1} in 100 × 70 μm (width × height) microchannel. Our experiments revealed an omnipresent trend in capture rate variation with flow: capture rates of different DNA molecules increased with increasing flow rates, reaching a DNA size-dependent maximum enhancement of 2.7–5.3× at moderate flow rates corresponding to a Peclet number of ~ $(4.05 \pm 0.05) \times 10^5$, then dropping upon further increasing the flow. We also examined the effect of flow in microchannels on the translocation time of DNA molecules. We showed that adjusting the flow rate and selectively exposing DNA to flow-induced viscous drag could be used to moderately tune the kinetics of DNA translocation. This could be beneficial to nanopore applications where the temporal resolution of measurements is affected by undesirably fast translocation events. To shed light on the physics underlying the experimentally observed trend in capture rate variation with flow velocity, we carried out numerical simulations to model DNA dynamics under the combined effect of Brownian motion, hydrodynamics force and electrophoretic drive. The simulations successfully reproduced the experimentally observed trend in capture rate variation with increasing flow velocity. They also revealed that the capture volume of a nanopore reduces in size and changes in shape from a hemisphere in the absence of flow to an asymmetric semi-ovoid skewed in the upstream direction in the presence of flow in microchannels. Force balance analysis on translocating DNA was also performed to establish a theoretical framework to explain the tunability of translocation kinetics observed in experiments. The predictions of simulations reconciled with experimental results, suggesting that the experimentally observed variations in DNA translocation time are generated by the drag force induced by flow on the translocating DNA.

4. EXPERIMENTAL SECTION

Silicon Chips: Silicon (Si) chips were purchased from Norcada (Norcada, NBPT005Z). They measure ~3 mm across and are comprised of a low-stress silicon nitride (SiN) film, with a nominal thickness of $l = 10 \pm 1$ nm, deposited over 200 μm thick silicon frame. A free standing SiN membrane with a size of 50×50 μm^2 is realized at the center of the chip through anisotropic etching of silicon frame. The chips were used, without any further treatment, in the fabrication of the test devices.

Integrated Nanopore-Microfluidic Test Device: The whole fabrication process was carried out in the cleanroom facility at the Godin Laboratory, University of Ottawa. The microchannel layers were prepared by casting degassed PDMS (Sylgard 184 kit, Dow Corning; mixed with 10:1 base to cross-linker ratio) on a silicon wafer master mold (same design used for top and bottom microchannels). The top and bottom via layers were prepared by spin coating degassed PDMS on silicon wafer master molds. PDMS layers were permanently bonded using air plasma (30 seconds, 50 Watts). To provide fluidic and electrical access to microchannels, holes were punched in PDMS using biopsy punches (0.75 mm for fluidic access, 1.25 mm for electrodes). Following the assembly of top and bottom PDMS pieces, the Si chip was bonded to the PDMS pieces using air plasma (18 seconds, 30 Watts) and then the gap left between the two PDMS pieces, i.e. around the Si chip, was filled with un-cured PDMS. Following a short bake in an oven set at 70 ºC, the integrated nanopore-microfluidic device was bonded to a glass slide to facilitate its handling through experiments. All microchannels have a rectangular cross section of width × height = 100×60 μm^2. The top channel includes a micro-via (length × width × height = 200×100×10 μm^3) above the nanopore which eventually increases the total microchannel height to 70 μm, as shown in the inset of Figure 1a and Figure S2a. Below the nanopore is a cylindrical fluidic via that measures 750 μm in diameter and 200 μm in height (20 μm for the experiments in

which DNA is sensed from the bottom side), Figure S2b. Further details of the fabrication process are discussed in Note 1, Supporting Information.

Fabrication, Enlargement (Conditioning) of Nanopore, Sensing: The integrated nanopore-microfluidic device was air plasma treated (24 seconds, 30 Watts) to render the microfluidic networks hydrophilic. Immediately after plasma treatment, microchannels were filled with deionized (DI) water under reduced pressure in a vacuum desiccator. Ag/AgCl electrodes were inserted into their corresponding punched holes, two on the top and one on the bottom side of the device, Figure 1. The device was mounted in a grounded metal box acting as a Faraday cage, Figure S3. The microchannels were interfaced with PEEK capillary tubing and briefly flushed with ethanol (5 minutes) to remove any trapped air bubbles from the electrodes. Next, the microchannels were rinsed with Deionized (DI) water (5-10 minutes), followed by filling with aqueous 1M KCl buffered with HEPES to pH 8. A ramped transmembrane bias voltage (ramp rate: 3 V/min up to 5 V, 0.75 V/min afterward) was applied to impose a high electric field across the SiN membrane. Custom-build electronic circuitry (co-hosted with the device in the Faraday cage) was used to apply the transmembrane voltage and to measure the resulting leakage current. The spontaneous creation of nanopore was perceived by a sudden increase in leakage current (threshold set at 10 nA). This generally resulted in the creation of a small nanopore (diameter < 4 nm) at a bias voltage of 7–10 V (dependent on membrane thickness and/or material composition). Next, moderate voltage pulses 3–4 V in amplitude were used to gradually enlarge the nanopore to its final targeted size of 6–10 nm (see Note 3, Supporting Information, for more details) [39]. During sensing experiments, the measurement of the ionic current passing through the nanopore was carried out using a single-channel patch-clamp amplifier (Axopatch 200B, Molecular Devices).

DNA samples: The bandwidth limitation of the patch-clamp amplifier imposes a temporal resolution of ~24 μs, making it somewhat challenging to characterize translocations of DNA molecules shorter than 1 kbp (see Note 2, Supporting Information, for more information). On the other hand, experiments with DNA molecules longer than 5 kbp (not shown here) demonstrated high sensitivity to cross-flow which resulted in frequent clogging, and hence shortened the lifetime of nanopores. Therefore, we limited our analysis to 1–5 kbp dsDNA, consistent with the DNA molecule sizes commonly used in solid-state nanopore experiments, e.g. 3–10 kbp in [40], 0.8–8 kbp in [20], and 0.5–10 kbp in [41].

DNA Sample Introduction: A pressure-driven Poiseuille flow was used to send DNA sample through the corresponding microchannel with a volumetric flow rate of $Q \sim 6\ \mu\mathrm{L/min}$ for about 5 minutes, followed by a 10 minutes wait time (2 hours for the experiment where DNA is introduced from the bottom side) for passive mixing to achieve homogenous DNA distribution (see Note 5, Supporting Information, for more details).

ASSOCIATED CONTENT

Supporting Information

Fabrication of devices; experimental setup and data acquisition; creation and tuning the size (conditioning) of nanopore; DNA sample preparation; flow rate control and measurement; uncertainty in the determination of characteristic flow velocity profile near nanopore; analysis of results; modeling and numerical simulations; kinetics of translocation in the presence of flow in microchannel.

AUTHOR INFORMATION

Notes

The authors declare no competing financial interest.

ACKNOWLEDGEMENTS

This work was supported by funding from the Natural Sciences and Engineering Research Council of Canada (NSERC) and the Canada Foundation for Innovation (CFI). The authors are grateful to Radin Tahvildari for assistance in the design of the prototype, Matthew Waugh for fruitful discussions on SiN membranes and Kyle Briggs for nanopore translocation analysis software.

REFERENCES

(1) Dekker, C. Solid-State Nanopores. *Nature Nanotech* **2007**, *2* (4), 209–215. https://doi.org/10.1038/nnano.2007.27.

(2) Branton, D.; Deamer, D. W.; Marziali, A.; Bayley, H.; Benner, S. A.; Butler, T.; Di Ventra, M.; Garaj, S.; Hibbs, A.; Huang, X.; Jovanovich, S. B.; Krstic, P. S.; Lindsay, S.; Ling, X. S.; Mastrangelo, C. H.; Meller, A.; Oliver, J. S.; Pershin, Y. V.; Ramsey, J. M.; Riehn, R.; Soni, G. V.; Tabard-Cossa, V.; Wanunu, M.; Wiggin, M.; Schloss, J. A. The Potential and Challenges of Nanopore Sequencing. *Nat Biotech* **2008**, *26* (10), 1146–1153. https://doi.org/10.1038/nbt.1495.

(3) Fologea, D.; Brandin, E.; Uplinger, J.; Branton, D.; Li, J. DNA Conformation and Base Number Simultaneously Determined in a Nanopore. *ELECTROPHORESIS* **2007**, *28* (18), 3186–3192. https://doi.org/10.1002/elps.200700047.

(4) Ma, J.; Qiu, Y.; Yuan, Z.; Zhang, Y.; Sha, J.; Liu, L.; Sun, L.; Ni, Z.; Yi, H.; Li, D.; Chen, Y. Detection of Short Single-Strand DNA Homopolymers with Ultrathin S i 3 N 4 Nanopores. *Phys. Rev. E* **2015**, *92* (2), 022719. https://doi.org/10.1103/PhysRevE.92.022719.

(5) Kwok, H.; Briggs, K.; Tabard-Cossa, V. Nanopore Fabrication by Controlled Dielectric Breakdown. *PLOS ONE* **2014**, *9* (3), e92880. https://doi.org/10.1371/journal.pone.0092880.

(6) Briggs, K.; Kwok, H.; Tabard-Cossa, V. Automated Fabrication of 2-Nm Solid-State Nanopores for Nucleic Acid Analysis. *Small* **2014**, *10* (10), 2077–2086. https://doi.org/10.1002/smll.201303602.

(7) Waugh, M.; Briggs, K.; Gunn, D.; Gibeault, M.; King, S.; Ingram, Q.; Jimenez, A. M.; Berryman, S.; Lomovtsev, D.; Andrzejewski, L.; Tabard-Cossa, V. Solid-State Nanopore Fabrication by Automated Controlled Breakdown. *Nat Protoc* **2020**, *15* (1), 122–143. https://doi.org/10.1038/s41596-019-0255-2.

(8) Tahvildari, R.; Beamish, E.; Tabard-Cossa, V.; Godin, M. Integrating Nanopore Sensors within Microfluidic Channel Arrays Using Controlled Breakdown. *Lab Chip* **2015**. https://doi.org/10.1039/C4LC01366B.

(9) Tahvildari, R.; Beamish, E.; Briggs, K.; Chagnon-Lessard, S.; Sohi, A. N.; Han, S.; Watts, B.; Tabard-Cossa, V.; Godin, M. Manipulating Electrical and Fluidic Access in Integrated Nanopore-Microfluidic Arrays Using Microvalves. *Small* **2017**, *13* (10), 1602601. https://doi.org/10.1002/smll.201602601.

(10) Hong, J. W.; Quake, S. R. Integrated Nanoliter Systems. *Nat Biotechnol* **2003**, *21* (10), 1179–1183. https://doi.org/10.1038/nbt871.

(11) Jiang, Y.; Zou, S.; Cao, X. Rapid and Ultra-Sensitive Detection of Foodborne Pathogens by Using Miniaturized Microfluidic Devices: A Review. *Anal. Methods* **2016**, *8* (37), 6668–6681. https://doi.org/10.1039/C6AY01512C.

(12) Shaqfeh, E. S. G. The Dynamics of Single-Molecule DNA in Flow. *Journal of Non-Newtonian Fluid Mechanics* **2005**, *130* (1), 1–28. https://doi.org/10.1016/j.jnnfm.2005.05.011.

(13) Sheehan, P. E.; Whitman, L. J. Detection Limits for Nanoscale Biosensors. *Nano Lett.* **2005**, *5* (4), 803–807. https://doi.org/10.1021/nl050298x.

(14) Squires, T. M.; Messinger, R. J.; Manalis, S. R. Making It Stick: Convection, Reaction and Diffusion in Surface-Based Biosensors. *Nat Biotechnol* **2008**, *26* (4), 417–426. https://doi.org/10.1038/nbt1388.

(15) Lynn, N. S.; Homola, J. (Bio)Sensing Using Nanoparticle Arrays: On the Effect of Analyte Transport on Sensitivity. *Anal. Chem.* **2016**, *88* (24), 12145–12151. https://doi.org/10.1021/acs.analchem.6b03002.

(16) Charron, M.; Briggs, K.; King, S.; Waugh, M.; Tabard-Cossa, V. Precise DNA Concentration Measurements with Nanopores by Controlled Counting. *Anal. Chem.* **2019**, *91* (19), 12228–12237. https://doi.org/10.1021/acs.analchem.9b01900.

(17) Di Carlo, D.; Irimia, D.; Tompkins, R. G.; Toner, M. Continuous Inertial Focusing, Ordering, and Separation of Particles in Microchannels. *Proceedings of the National Academy of Sciences* **2007**, *104* (48), 18892–18897. https://doi.org/10.1073/pnas.0704958104.

(18) Ismagilov, R. F.; Stroock, A. D.; Kenis, P. J. A.; Whitesides, G.; Stone, H. A. Experimental and Theoretical Scaling Laws for Transverse Diffusive Broadening in Two-Phase Laminar

Flows in Microchannels. *Appl. Phys. Lett.* **2000**, *76* (17), 2376–2378. https://doi.org/10.1063/1.126351.

(19) Zheng, X.; Silber-Li, Z. Measurement of Velocity Profiles in a Rectangular Microchannel with Aspect Ratio α = 0.35. *Exp Fluids* **2008**, *44* (6), 951–959. https://doi.org/10.1007/s00348-007-0454-4.

(20) Wanunu, M.; Morrison, W.; Rabin, Y.; Grosberg, A. Y.; Meller, A. Electrostatic Focusing of Unlabelled DNA into Nanoscale Pores Using a Salt Gradient. *Nature Nanotech* **2010**, *5* (2), 160–165. https://doi.org/10.1038/nnano.2009.379.

(21) Grosberg, A. Y.; Rabin, Y. DNA Capture into a Nanopore: Interplay of Diffusion and Electrohydrodynamics. *The Journal of Chemical Physics* **2010**, *133* (16), 165102. https://doi.org/10.1063/1.3495481.

(22) Qiao, L.; Slater, G. W. Capture of Rod-like Molecules by a Nanopore: Defining an "Orientational Capture Radius." *J. Chem. Phys.* **2020**, *152* (14), 144902. https://doi.org/10.1063/5.0002044.

(23) Mihovilovic, M.; Hagerty, N.; Stein, D. Statistics of DNA Capture by a Solid-State Nanopore. *Phys. Rev. Lett.* **2013**, *110* (2), 028102. https://doi.org/10.1103/PhysRevLett.110.028102.

(24) Briggs, K.; Charron, M.; Kwok, H.; Le, T.; Chahal, S.; Bustamante, J.; Waugh, M.; Tabard-Cossa, V. Kinetics of Nanopore Fabrication during Controlled Breakdown of Dielectric Membranes in Solution. *Nanotechnology* **2015**, *26* (8), 084004. https://doi.org/10.1088/0957-4484/26/8/084004.

(25) Meller, A.; Branton, D. Single Molecule Measurements of DNA Transport through a Nanopore. *ELECTROPHORESIS* **2002**, *23* (16), 2583–2591. https://doi.org/10.1002/1522-2683(200208)23:16<2583::AID-ELPS2583>3.0.CO;2-H.

(26) Briggs, K.; Madejski, G.; Magill, M.; Kastritis, K.; de Haan, H. W.; McGrath, J. L.; Tabard-Cossa, V. DNA Translocations through Nanopores under Nanoscale Preconfinement. *Nano Lett.* **2018**, *18* (2), 660–668. https://doi.org/10.1021/acs.nanolett.7b03987.

(27) Roy, B.; Das, T.; Maiti, T. K.; Chakraborty, S. Effect of Fluidic Transport on the Reaction Kinetics in Lectin Microarrays. *Analytica Chimica Acta* **2011**, *701* (1), 6–14. https://doi.org/10.1016/j.aca.2011.05.049.

(28) Beamish, E.; Tabard-Cossa, V.; Godin, M. Programmable DNA Nanoswitch Sensing with Solid-State Nanopores. *ACS Sens.* **2019**, *4* (9), 2458–2464. https://doi.org/10.1021/acssensors.9b01053.

(29) Verschueren, D. V.; Jonsson, M. P.; Dekker, C. Temperature Dependence of DNA Translocations through Solid-State Nanopores. *Nanotechnology* **2015**, *26* (23), 234004. https://doi.org/10.1088/0957-4484/26/23/234004.

(30) Wanunu, M.; Sutin, J.; McNally, B.; Chow, A.; Meller, A. DNA Translocation Governed by Interactions with Solid-State Nanopores. *Biophysical Journal* **2008**, *95* (10), 4716–4725. https://doi.org/10.1529/biophysj.108.140475.

(31) Volpe, G.; Gigan, S.; Volpe, G. Simulation of the Active Brownian Motion of a Microswimmer. *American Journal of Physics* **2014**, *82* (7), 659–664. https://doi.org/10.1119/1.4870398.

(32) Muthukumar, M. *Polymer Translocation*; Taylor & Francis: Boca Raton, 2011 (p.252).

(33) Robertson, R. M.; Smith, D. E. Strong Effects of Molecular Topology on Diffusion of Entangled DNA Molecules. *Proceedings of the National Academy of Sciences* **2007**, *104* (12), 4824–4827. https://doi.org/10.1073/pnas.0700137104.

(34) Freedman, K. J.; Otto, L. M.; Ivanov, A. P.; Barik, A.; Oh, S.-H.; Edel, J. B. Nanopore Sensing at Ultra-Low Concentrations Using Single-Molecule Dielectrophoretic Trapping. *Nat Commun* **2016**, *7* (1), 10217. https://doi.org/10.1038/ncomms10217.

(35) Storm, A. J.; Storm, C.; Chen, J.; Zandbergen, H.; Joanny, J.-F.; Dekker, C. Fast DNA Translocation through a Solid-State Nanopore. *Nano Lett.* **2005**, *5* (7), 1193–1197. https://doi.org/10.1021/nl048030d.

(36) Batchelor, G. K. Slender-Body Theory for Particles of Arbitrary Cross-Section in Stokes Flow. *J. Fluid Mech.* **1970**, *44* (3), 419–440. https://doi.org/10.1017/S002211207000191X.

(37) Perkins, T.; Quake; Smith, D.; Chu, S. Relaxation of a Single DNA Molecule Observed by Optical Microscopy. *Science* **1994**, *264* (5160), 822–826. https://doi.org/10.1126/science.8171336.

(38) Marko, J. F.; Siggia, E. D. Stretching DNA. *Macromolecules* **1995**, *28* (26), 8759–8770. https://doi.org/10.1021/ma00130a008.

(39) Beamish, E.; Kwok, H.; Tabard-Cossa, V.; Godin, M. Precise Control of the Size and Noise of Solid-State Nanopores Using High Electric Fields. *Nanotechnology* **2012**, *23* (40), 405301. https://doi.org/10.1088/0957-4484/23/40/405301.

(40) Li, J.; Gershow, M.; Stein, D.; Brandin, E.; Golovchenko, J. A. DNA Molecules and Configurations in a Solid-State Nanopore Microscope. *Nature Mater* **2003**, *2* (9), 611–615. https://doi.org/10.1038/nmat965.

(41) Bell, N. A. W.; Muthukumar, M.; Keyser, U. F. Translocation Frequency of Double-Stranded DNA through a Solid-State Nanopore. *Phys. Rev. E* **2016**, *93* (2), 022401. https://doi.org/10.1103/PhysRevE.93.022401.

FOR TABLE OF CONTENT ONLY

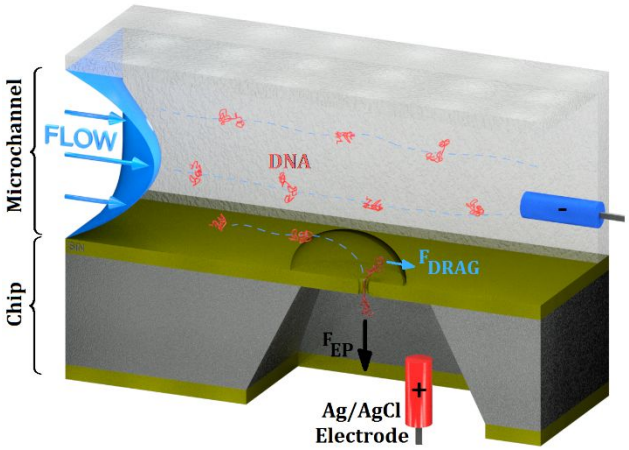
Microchannel
FLOW
DNA
Chip
F_{DRAG}
F_{EP}
Ag/AgCl
Electrode
-
+

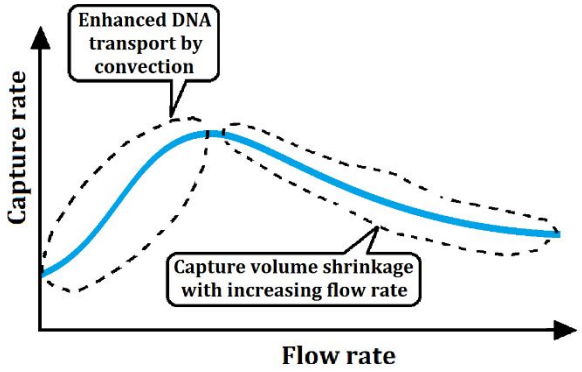
Enhanced DNA transport by convection
Capture rate
Capture volume shrinkage with increasing flow rate
Flow rate